

1 Generative AI for image reconstruction in Intensity Interferometry: a first attempt

2 KM NITU RAI,^{1,2} YURI VAN DER BURG,³ SOUMEN BASAK,¹ PRASENJIT SAHA,³ AND SUBRATA SARANGI^{4,5}

3 ¹*School of Physics, Indian Institute of Science Education and Research Thiruvananthapuram, Maruthamala PO, Vithura,*
4 *Thiruvananthapuram 695551, Kerala, India.*

5 ²*Aryabhatta Research Institute of Observational Sciences, Manora Peak, Nainital 263129, India.*

6 ³*Physik-Institut, University of Zurich, Winterthurerstrasse 190, 8057 Zurich, Switzerland.*

7 ⁴*School of Applied Sciences, Centurion University of Technology and Management, Odisha-752050, India.*

8 ⁵*Visiting Associate, Inter-University Centre for Astronomy and Astrophysics, Post Bag 4, Ganeshkhind, Pune 411 007, Maharashtra,*
9 *India.*

ABSTRACT

In the last few years Intensity Interferometry (II) has made significant strides in achieving high-precision resolution of stellar objects at optical wavelengths. Despite these advancements, phase retrieval remains a major challenge due to the nature of photon correlation. This paper explores the application of a conditional Generative Adversarial Network (cGAN) to tackle the problem of image reconstruction in II. This method successfully reconstructs the shape, size, and brightness distribution of simulated, fast-rotating stars based on a sparsely sampled spatial power spectrum obtained from a hypothetical ground-based II facility composed of four Imaging Atmospheric Cherenkov Telescopes (IACTs). Although this particular example could also be addressed using parameter fitting, the results suggest that with larger arrays much more complicated systems could be reconstructed by applying machine-learning techniques to II.

20 1. INTRODUCTION

21 Humans instinctively feel a relationship with the stars.
22 One of the primary scientific projects of humanity is to
23 figure out what the stars are and how do they do what
24 they do. The first obvious step in this project, beyond
25 measuring their global parameters like diameter, mass,
26 orbital and astrometric elements, is to obtain images of
27 the stars with all details of the stellar surfaces. In case
28 of the Sun, this is done routinely by observatories and
29 sun-observation satellites. But such routine still remains
30 a challenge even for the α -centauri system, our nearest
31 stellar neighbour. The objective is to achieve capability
32 of high fidelity image reconstruction of distant stars.
33 Two interferometry based techniques, namely, Michelson
34 Interferometry (MI) or Intensity Interferometry (II)
35 have emerged during the last century to address this
36 objective. A discussion of the development of these two
37 approaches and comparison of their respective merits
38 and challenges can be found in (K. N. Rai et al. 2025).
39 The work reported here presents the results of a first
40 effort at applying a Conditional Generative Adversarial
41 (neural) Network (cGAN) to image reconstruction of a
42 fast rotator using its simulated II observations.

43 The foundational basis of II stems from the pioneering
44 experiments and theoretical investigations, widely
45 referred to as the “HBT effect”, carried out initially by

46 Hanbury Brown and Twiss (HBT) R. Hanbury Brown
47 & R. Q. Twiss (1956); R. Hanbury Brown et al. (1957,
48 1958) and, later, by Glauber (R. J. Glauber 1963). The
49 correlation between photons (called HBT effect) measured
50 by a pair of photon detectors in two coherent
51 beams of light was reported in 1956 R. Hanbury Brown
52 & R. Q. Twiss (1956). K. N. Rai et al. (2025) present
53 a modern-day variant of this experiment, carried out
54 with pseudo-thermal light. The HBT Effect and the re-
55 lated theoretical investigations laid the foundation for
56 the modern field of Quantum Optics.

57 Hanbury Brown and his collaborators led the creation
58 and installation of the iconic II facility at Narrabri, Aus-
59 tralia and reported the measurement of angular diame-
60 ters of 32 stars and a few multiple star-systems (R. Han-
61 bury Brown et al. 1974). Soon after this work, however,
62 II observations of stars was stalled for over four decades
63 due to the limits of the then available photon detectors
64 and data processing equipment. With gradual mitiga-
65 tion of such issues, proposals to utilize Imaging Atmo-
66 spheric Cherenkov Telescope (IACT) facilities for con-
67 ducting II observations of stars have emerged (J. Le Bo-
68 hec 2006; P. D. Nuñez et al. 2010, 2012a; D. Dravins et
69 al. 2013) as a secondary science application of these fa-
70 cilities during moonlit nights. SII observations at VER-
71 ITAS, MAGIC, and HESS are now being reported (e.g.,

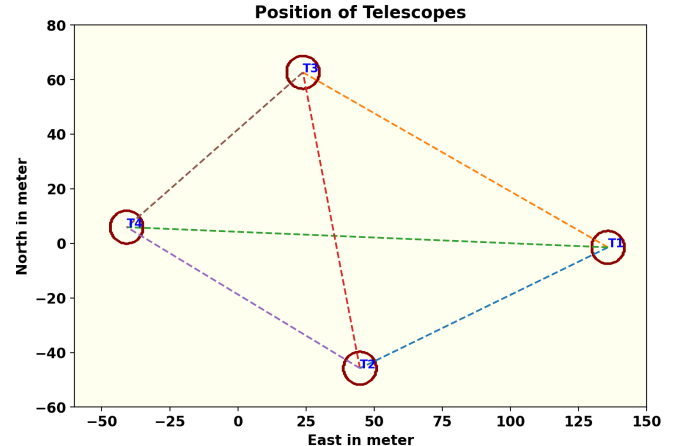


Figure 1. A schematic representation of a hypothetical observation facility with an array of four Cherenkov Telescopes (IACTs) whose relative positions approximately mimic those at VERITAS. This array is used in simulating the Intensity Interferometry (II) observation of the fast rotators. Each of the telescopes has a diameter of 12m. The baselines provided by the array are of the order of 100m.

A. Acharyya et al. 2024; S. Abe et al. 2024; N. Vogel et al. 2025). This approach has the potential to enhance the scientific output of existing IACT facilities, and especially of the upcoming Cherenkov Telescope Array Observatory (CTAO). Simulations carried out by Rai et al. (K. N. Rai et al. 2021, 2022, e.g.,) have shown that recent advancements in photon detectors could be effective in achieving high-precision measurements of parameters for stellar objects.

The thrust of these efforts has been to measure the average global parameters of stars and star systems. The high fidelity imagery, however, would transcend the measurement of global and average stellar parameters, such as angular diameters, binary separations, and orbital characteristics, which offer only an integrated view of the star or star system as a whole. Such imaging capabilities promise direct insights into the dynamic surface phenomena, including limb darkening, convection cells, granulation, star spots, oblateness and gravity darkening in rapid rotators and atmospheric structures, akin to the detailed observations routinely conducted on our own Sun.

As it stands today, studies grappling various issues of image reconstruction are being reported (X. Haubois et al. 2009; R. P. Norris et al. 2021; L.-C. Liu et al. 2024; L.-C. Liu et al. 2025). MI-based image reconstruction has made substantial progress in this area with efforts at generating constructed images of stars like Betelgeuse (X. Haubois et al. 2009) and AZ Cyg (R. P. Norris et al. 2021). On the other hand, II-based methods are in a nascent stage. The recent publications L.-C. Liu et al. (2024); L.-C. Liu et al. (2025) have demonstrated, through outdoor experiments, imaging millimeter-scale targets at 1.36 km with a resolution 14 times better than a single telescope's diffraction limit. A "flexible computational algorithm" reconstructs images from intensity correlations, overcoming atmospheric turbulence and optical imperfections.

We report here, the results of our attempt – the first of its kind – to construct the gravity-darkened sky-image of fast rotating stars consistent with their respective simulated ground-based II-observations using a cGAN neural network architecture. Image reconstruction in gravity darkened fast rotating stars has long been examined using various methods in MI (G. T. van Belle et al. 2001; A. Domiciano de Souza et al. 2003, 2005; H. A. McAlister et al. 2005; J. D. Monnier et al. 2007; E. Pedretti et al. 2009; M. Zhao et al. 2009; A. O. Martinez et al. 2021). Recently photosphere oblateness of γ -Cassiopeia (A. Archer et al. 2025) has been measured at the VERITAS observatory using II. These results, and especially, that by A. Archer et al. (2025) put our work in con-

text. Thus our work presented here is a natural next step of the work of Archer et al and others. We emulate the cGAN model P. Isola et al. (2017) to reconstruct images of fast-rotating stars using their simulated Intensity Interferograms and sky-intensity distributions as input data for training, testing, and validation. We consider an array of four Imaging Cherenkov Telescopes (IACTs) whose relative positions approximately mimic those at VERITAS and simulate observations of a set of synthetically generated fast-rotating stars. The image predicted by the trained cGAN shows promising results in reconstructing the stars' shapes and sizes. The reconstructed brightness distributions are then assessed using moments.

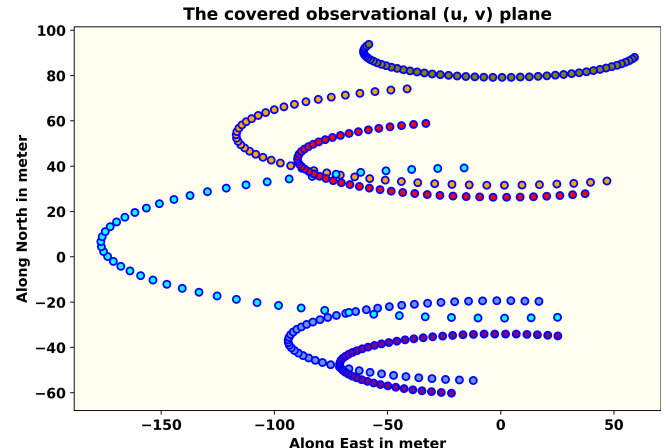
This paper is organized as follows. The next section discusses briefly the past efforts at image reconstruction on II, followed by the section on a discussion of Intensity Interferometry, focusing on its signal and noise characteristics for fast-rotating stars along the Earth's rotation. The following section introduces the cGAN formulation and its structure. The fifth section details the parameter selection for training the network for image reconstruction. The sixth section presents the results of the trained network both visually and via image moments. Finally, the paper concludes with a discussion of the overall results.

151 2. PAST EFFORTS AT IMAGE
 152 RECONSTRUCTION IN INTENSITY
 153 INTERFEROMETRY

154 Several approaches have been developed for phase re-
 155 construction in intensity interferometry (II). H. Gamo
 156 (1963) introduced triple-intensity correlation, applied by
 157 M. L. Goldberger et al. (1963) to microscopic systems
 158 and extended by T. Sato et al. (1978, 1979, 1981) to
 159 measure stellar diameters and phases, though limited
 160 by low signal-to-noise ratio (SNR). R. W. Gerchberg
 161 (1972) proposed an iterative phase retrieval method us-
 162 ing image and diffraction plane data, sensitive to initial
 163 estimates and convergence speed. J. Fienup (1982) im-
 164 proved this with the Hybrid Input-Output algorithm,
 165 enhancing robustness in noisy conditions. R. Holmes et
 166 al. (2010) utilized Cauchy-Riemann relations for 1-D
 167 and 2-D image reconstruction, applied to simulated
 168 stellar data with Imaging Cherenkov Telescope Arrays
 169 (P. D. Nuñez et al. 2010, 2012a,b), but faced compu-
 170 tational complexity for higher dimensions. X. Li et al.
 171 (2014) introduced a regularized iterative method incor-
 172 porating priors (e.g., sparsity) to mitigate noise and
 173 ill-posedness, though challenged by parameter tuning
 174 and initial guess sensitivity. The Transport-of-Intensity
 175 Equation (TIE), proposed by M. R. Teague (1983), re-
 176 trievals phase from intensity variations across planes;
 177 J. Zhang et al. (2020) solved TIE as a Poisson equa-
 178 tion using a maximum intensity assumption, while C.
 179 Kirisits et al. (2024) combined TIE with the Trans-
 180 port of Phase Equation for improved accuracy across
 181 arbitrary apertures and non-uniform illumination, with
 182 convergence dependent on initial guesses and boundary
 183 conditions.

184 With non-linearity built into their architecture, artifi-
 185 cial neural networks (ANNs) empowered by deep learn-
 186 ing methods are promising for exploring the task of re-
 187 constructing images of stellar objects from ground-based
 188 observations. Convolutional Neural Networks (CNNs),
 189 with their specialized architecture for processing two-
 190 dimensional datasets, are a natural choice for image
 191 processing tasks. In astronomical image reconstruction
 192 projects, a common challenge is that the interferometric
 193 data are typically undersampled as well as noisy. There-
 194 fore, the CNN architectures and deep learning methods
 195 employed must be capable of reliably learning both the
 196 global context of the training dataset and the local fea-
 197 tures within it. Among the various CNN architectures,
 198 U-Net models (O. Ronneberger et al. 2015) have proven
 199 successful in such tasks.

200 Furthermore, given that achieving a high signal-to-
 201 noise ratio (SNR) is often challenging in astronomical
 202 datasets, it is immensely beneficial if additional data can



203 **Figure 2.** The tracks of the baselines due to Earth ro-
 204 tation (described in sec. 3.3) provided by the hypothetical
 205 observation facility of four telescopes arranged in fig. 1 for
 206 one night of observation. The number of baselines scales as
 207 square of number of telescopes in the array thus leading to
 208 greater coverage of the observational plane and better image
 209 reconstruction prospects.

210 be generated using the available information from the
 211 observed sky density distribution and ground-based ob-
 212 servations (II data, in our case) of the sources under in-
 213 vestigation. Generative Adversarial Networks (GANs),
 214 introduced by I. Goodfellow et al. (2014), have been
 215 successful in such data augmentation tasks. Conditional
 216 GAN (cGAN) architectures, proposed by M. Mirza et al.
 217 (2014) and applied to a wide variety of datasets by P.
 218 Isola et al. (2017), leverage additional information about
 219 the images in the training datasets and have demon-
 220 strated remarkable robustness in image recovery across
 221 diverse data types.

222 In the astrophysical context, K. Schawinski et al.
 223 (2017) employed a GAN model to recover features —
 224 such as spiral arms, central bulges, and disk structures
 225 of galaxies — from noise-affected images. M. Mustafa et
 226 al. (2019) developed and customized a Deep Convo-
 227 lutional GAN, dubbed “CosmoGAN”, capable of gen-
 228 erating high-fidelity weak-lensing convergence maps of
 229 dark matter distribution that statistically reproduce real
 230 weak lensing structures. D. Coccolini et al. (2021)
 231 have successfully generated credible images of planets,
 232 nebulae, and galaxies using “lightweight” and “physics-
 233 uninformed” GANs to produce synthetic images of cele-
 234 stial bodies. They also generated a “Hubble Deep Field-
 235 inspired” wide-view simulation of the universe.

236 3. INTENSITY INTERFEROMETRY (II) WITH
 237 IACT ARRAYS

238 This section presents a brief conceptual overview of
 239 how an array of telescopes is used to perform II obser-

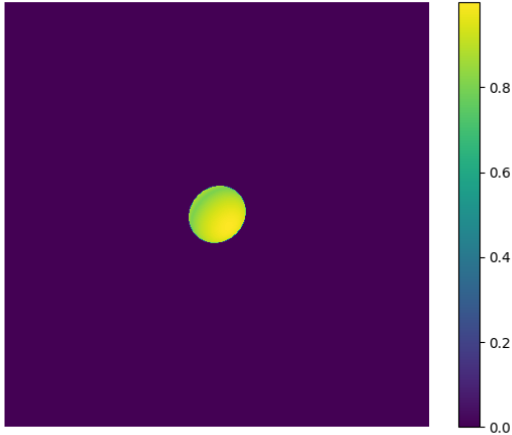


Figure 3. This figure shows one of the simulated fast rotating stars (FRS). The brightness is highest at the poles; gravity darkening visible along the equator. A total of 31460 such images of FRS with different parameter values have been generated to train the model.

vations, and explains the Signal-to-Noise Ratio (SNR) from these measurements.

3.1. The signal for II

As a simple example, let us consider a pair of IACTs pointed at a star. Suppose the two telescopes simultaneously measure the intensity of radiation $I_1(t)$ and $I_2(t)$, respectively. The signals from these detectors are cross-correlated and averaged over time, yielding the second order ($n = 2$) correlation of these intensities as (cf. V. A. Acciari et al. 2020; D. Dravins et al. 2013)

$$g^{(2)} = \frac{\langle I_1(t) \cdot I_2(t + \tau) \rangle}{\langle I_1(t) \rangle \cdot \langle I_2(t) \rangle} \quad (1)$$

where τ is the time delay between the telescopes. For spatially coherent and randomly polarized light, Eq. (1) reduces to the relation (sometimes called the Siegert relation, see e.g., V. A. Acciari et al. 2020).

$$g^{(2)} = 1 + \frac{\Delta f}{\Delta \nu} |V_{12}|^2 \quad (2)$$

where Δf is the electronic bandwidth of the photon detectors which measure the intensities and $\Delta \nu$ is the frequency bandwidth of the filters employed in the telescopes to observe the star. Values of $\Delta \nu \sim 1$ THz and $\Delta f \sim 1$ GHz are typical of recent work. In Eq. (2), V_{12} , referred to as the complex visibility function, is the Fourier transform of the source brightness distribution. It contains information about the star's angular diameter. However, the phase information is lost since we measure only the absolute value $|V_{12}|^2$. In observational

astronomy, the correlation is often expressed in terms of the normalized contrast, given by:

$$c = g^{(2)} - 1 = \frac{\Delta f}{\Delta \nu} |V_{12}|^2 \quad (3)$$

with $|V_{12}|^2$ being a function of baseline $b = \sqrt{u^2 + v^2}$ on the observational plane (u, v) . This implies the strength of the signal would be enhanced if a larger number of baselines or pairs of telescopes are employed.

3.2. The Signal-to-Noise Ratio for II

The primary purpose of IACTs is to study high-energy gamma rays (with energy $E \geq 30$ GeV) arriving from cosmic sources, entering the Earth's atmosphere, and initiating Cherenkov showers in the upper atmosphere due to multiple scattering. These telescopes feature an array of mirrors that focus light received from a sky source onto their respective set of photo-multiplier tubes (PMTs, see e.g., J. Aleksić et al. 2016) with appropriate specifications needed for II observations. In the simulation model adopted here, we consider a set of four IACTs, each with similar properties. The positional configuration of these IACTs is shown in Fig. 1. The optical signal directed to a PMT is filtered using a spectral filter with a chosen mean observational wavelength λ and corresponding bandpass $\Delta \lambda$. The use of filters not only reduces background noise but also improves the signal quality and the efficiency of the PMTs. Filtering background skylight becomes even more significant in II observations, as, currently, these are carried out during full moon nights when the primary function of the IACTs (of observing Cherenkov Showers) is rendered infeasible. It is important to note that the light from the stellar source is focused on a PMT attached with each of the telescopes during II observations.

The significance of the signal can be expressed in terms of the signal-to-noise ratio (SNR), which depends on many factors. However, most importantly, it does not depend on the optical bandwidth $\Delta \nu$ of the radiation for a two-telescope correlation. The explanation for the independence of the SNR from $\Delta \nu$ is provided in several works (e.g., subsection 4.1 of K. N. Rai et al. 2021). The Signal-to-Noise is given by

$$SNR = A \cdot \alpha \cdot q \cdot n \cdot F^{-1} \cdot \sigma \cdot \sqrt{\frac{T \Delta f}{2}} \cdot |V_{12}|^2 \quad (4)$$

Here, A is the total mirror area, α is the quantum efficiency of the PMTs, q is the throughput of the remaining optics, and n is the differential photon flux from the source. The excess noise factor of the PMTs is represented by F , T denotes the observation time, and σ is the normalized spectral distribution of the light (including filters) (e.g., V. A. Acciari et al. 2020).

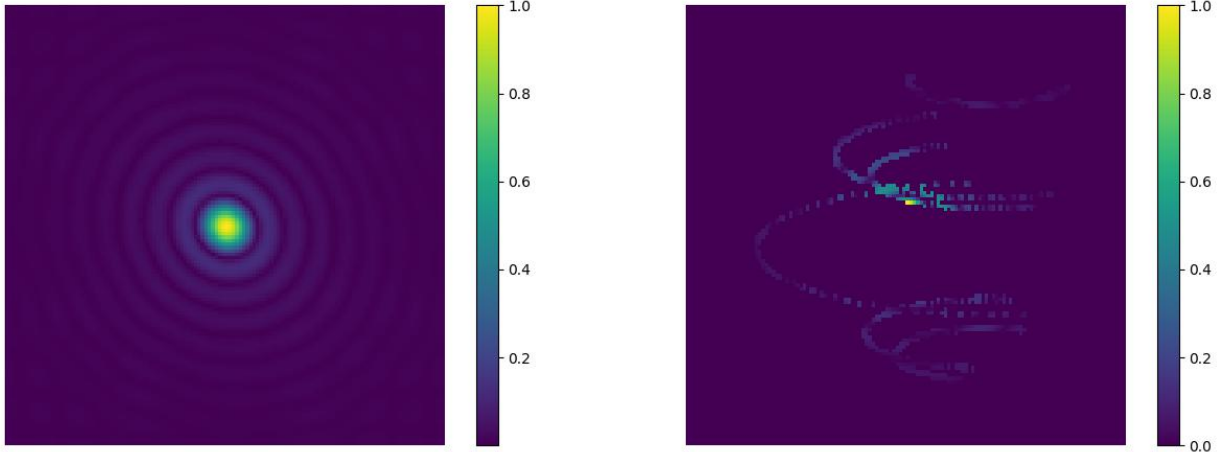


Figure 4. The left panel shows the absolute value of the two-dimensional Fast Fourier Transform of the source depicted in Fig. 3. It represents the intensity interferometric (u, v) plane image of the source that would be obtained by an infinite number of baselines (or an infinite number of telescopes observing the source). The right panel shows the absolute value of the same source measured along the tracks shown in Fig. 2. This figure reflects the sparse nature of the signal received by a realistic finite number of telescopes and baselines sampled from the full (u, v) plane signal space, as shown in the figure on the left panel. Both figures are plotted on a linear scale and normalized to the maximum pixel value in each respective figure.

3.3. Baseline considerations

The measurement of the size of stellar objects via squared visibility depends on the distance between the telescopes, known as the baseline b .

$$|V_{12}(b)|^2 = \frac{c(b)}{c(0)} \quad (5)$$

For achieving a good SNR with a given telescope configuration, covering as much as possible of the interferometric plane is always desirable. If the source is at the zenith, the coordinates in the Fourier plane (u, v) are given by:

$$(u, v) = \frac{1}{\lambda} (b_E, b_N) \quad (6)$$

where b_E and b_N are, respectively, the baselines expressed in east and north coordinates. However, the sources can be anywhere on the sky, and the telescopes are stationary and may also have different relative altitudes b_A depending on the available terrain. In order to gather maximum possible information on the source during the observation session and to cover as much of the observational plane as possible during such sessions, Earth's rotation must be taken into account using rotated baselines. For a given stellar source with declination δ and hour-angle h , as observed by telescopes located at latitude l , equation (7) provides the rotated baselines for a given pair of telescopes (see e.g., eqs. 8–10 from S. Baumgartner et al. 2020) with the R -matrices

representing the respective rotation operations.

$$\begin{pmatrix} u \\ v \\ w \end{pmatrix} = R_x(\delta) \cdot R_y(h) \cdot R_x(-l) \begin{pmatrix} b_E \\ b_N \\ b_A \end{pmatrix} \quad (7)$$

Fig. 2 shows the track of six baselines generated from the telescopes (Fig. 1) due to the Earth's rotation. Since every pair of telescopes traces an ellipse in the Fourier plane, the total number of ellipses scales as

$$\mathcal{N} = \frac{1}{2} N_T \cdot (N_T - 1) \quad (8)$$

where N_T is the number of telescopes considered. As the number of baselines increases non-linearly, Intensity Interferometry (II) benefits greatly from a large number of telescopes. The CTAO can offer many more baselines — D. Dravins et al. (2013) considered the telescope configurations then being planned and showed how it would provide a dense coverage of the interference plane.

3.4. A Fictitious Fast Rotating Star: Our Test Case

In our work presented here, we attempt image reconstruction of a fast-rotating star using its simulated Intensity Interferometric observation in a cGAN architecture. Fast-rotating stars are important test cases for understanding various astrophysical processes, including stellar evolution, internal structure, and dynamical behaviour over time. Fast rotation causes stars to adopt an oblate shape, flattening at the poles and bulging at the equator due to the stronger centrifugal force (e.g., H. Von Zeipel 1924; A. Maeder 1999). Fig. 3 shows an

image qualitatively representing a fictitious fast-rotating star, with brightness (and, therefore, the effective surface temperature) distributed across its surface. The brightness (effective temperature) is highest at the poles and lowest at the equator, a phenomenon known as gravity darkening (L. B. Lucy 1967). First direct interferometric detection of stellar photospheric oblateness (of Altair) was pioneered by van Belle et al G. T. van Belle et al. (2001) using the Palomar Testbed Interferometer (PTI) and the Navy Prototype Optical Interferometer (NPOI). Gravity darkening due to fast rotation was first observed through interferometric and spectroscopic data from the CHARA Array for the fast-rotating star Regulus (H. A. McAlister et al. 2005). As pointed out earlier, these two pieces of work, all using Michelson Interferometry, make a subset of several others (G. T. van Belle et al. 2001; A. Domiciano de Souza et al. 2003; H. A. McAlister et al. 2005; A. Domiciano de Souza et al. 2005; J. D. Monnier et al. 2007; E. Pedretti et al. 2009; M. Zhao et al. 2009; A. O. Martinez et al. 2021). The first observation of photospheric oblateness (of γ Cassiopeiae or γ -Cas) using Intensity Interferometry (II) has been recently carried out at VERITAS observatory and is reported by Archer et al. A. Archer et al. (2025). Reportage of such observations of other γ -Cas like targets and other class of FRS by Cherenkov Telescope arrays, such as the MAGIC array, are expected by 2026. In addition, observation and measurement of gravity darkening using II is the natural next step and is yet to be reported. In this context, our work of reconstructing the image of FRSs from their II-simulated observations using cGAN is an attempt at solving this inverse problem along with mitigation of loss of phase information in II.

Intensity Interferometry counts the photons arriving at the telescopes from the stellar object. The correlation of these photon arrivals at the telescopes yields the squared visibility Eq. (5), as explained in subsection 3.1. The left panel of fig. 4 shows the signal from the source shown in Fig. 3 using II, displayed on linear scales. Point to note here is that this figure represents the signal from the source that would be recorded by an infinite number of baselines provided by an infinite number of telescopes on the interferometric plane. In practice, only a small part of this information is available (as seen in right panel of Fig. 4), because one has a finite number of baselines corresponding to the finite number N_T of telescopes at our disposal and a limited observation schedule. We have simulated the II observation of the fictitious star by a hypothetical observation facility having an array of four IACTs with their relative positions approximating those at VERITAS (correlated

with baselines as seen in Fig. 1) over one night. Using this modest amount of signal from one night's observation, we have trained a cGAN to construct the image of the source.

4. GENERATIVE ADVERSARIAL NETWORKS

Generative Adversarial Networks (GANs) were introduced by I. Goodfellow et al. (2014). A GAN model involves two competing deep neural network models, referred to as the Generator and the Discriminator. These two networks engage in a zero-sum “Minimax” game, as in the Game Theory. Given a real data set $\{x_i\}$ (for example, a set of real images) drawn from some unknown distribution $P_{\text{data}}(x)$ generated by some unknown or ill-understood process, the objective here is to generate a new set (of images) whose probability distribution should match $P_{\text{data}}(x)$ as closely as possible. During the training of the two models, the Generator samples a latent variable z from a known prior distribution $P_z(z)$ (e.g., the Normal Distribution) and produces a synthetic sample $G(z)$ to start with and, subsequently, based on updates received from the Discriminator as its training progresses. The Discriminator, being a probabilistic binary classifier, receives either a real data sample x or a generated sample $G(z)$, and outputs a probability that the input is real. The Discriminator aims to maximise its classification accuracy, while the Generator aims to fool it by trying to minimize it. The training of these two networks proceeds alternately leading to the optimization of the adversarial loss function $L(D, G)$ given by

$$\begin{aligned} L(D, G) &= \min_G \max_D V(D, G) \\ &= \mathbb{E}_{x \sim p_{\text{data}}(x)} [\log D(x)] \\ &\quad + \mathbb{E}_{z \sim p_z(z)} [\log (1 - D(G(z)))] . \end{aligned} \quad (9)$$

The two neural networks $G(z) \equiv G(z; \theta_G)$ and $D(x) \equiv D(x; \theta_D)$ are parameterized by θ_i with $i = G$ or D respectively. During its training, the Generator generates the differentiable function $x_{\text{gen}} \equiv G(z)$ that maps z to the data space x . Through such maps the Generator generates its own distribution $p_G(x_{\text{gen}})$ and through the training episodes, specifically by iteratively updating its parameters θ_G , aligns this distribution with the distribution of real data $p_{\text{data}}(x)$. The training data set provided to the Discriminator is constructed by mixing real data points x and generated data points x_{gen} in equal ratio. The Discriminator generates the function $D(x)$ that represents the probability that x originates from real data. Eq.(9) implies that training of the GAN model moves towards maximization of the expectation of $D(x)$. Through this process, both the parameters θ_G

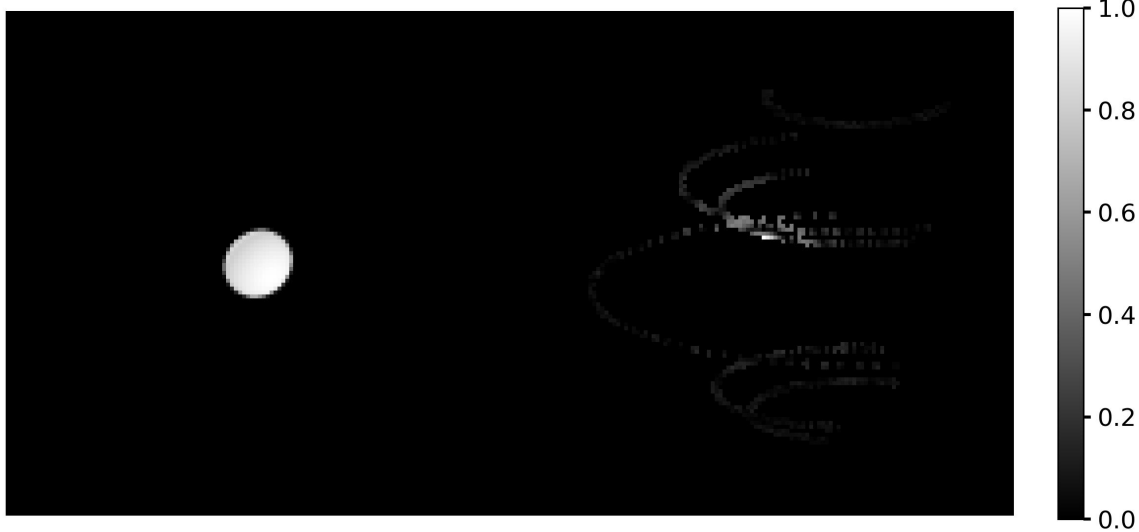


Figure 5. An illustrative example of the input used for training the cGAN model. The picture on the left shows the source image, which serves as the ground truth or the real data (x , as mentioned in the Flow Diagram (Fig. 6 discussed later during the training. The picture on the right represents the simulated Intensity Interferometry (II) observation pattern of the source (on the left) using a hypothetical observation facility having as array of four IACTs (see Fig. 1) and the tracks of the six telescope baselines (see Fig. 2) generated by these four IACTs due to Earth’s rotation during the observation session. This pattern referred to as y , in the Flow Diagram (Fig. 6 discussed later forms the “condition” during the training to which the GAN model has to conform. Salt-and-pepper noise is added to this pattern for enhancing the robustness of the cGAN model. Together, these images form a training pair, where the GAN learns to reconstruct a predicted image (modeling of observed signal) similar to ground truth (left) from the noisy baseline signal (right). The grayscale in both images is normalized to the brightest pixel.

and θ_D are optimized such that $p_G(x_{gen})$ gets maximally aligned with $p_{data}(x)$.

For a given fixed Generator $G(z)$, the problem can be reformulated as:

$$\max_D V(D, G) = \mathbb{E}_{x \sim p_{data}} [\log D_G^*(x)] + \mathbb{E}_{x \sim p_G} [\log (1 - D_G^*(x))] \quad (10)$$

where D_G^* denotes the optimum of the discriminator. As seen in equation (11), the global optimum of equation (10) is achieved if and only if $p_G = p_{data}$. Furthermore, if both G and D are allowed to reach their respective optima, – the so called Nash point of the Minimax game – p_G converges to p_{data} .

$$D_G^*(x) = \frac{p_{data}(x)}{p_{data}(x) + p_G(x_{gen})} \quad (11)$$

At this point, the Discriminator finds its job no better than random guessing. A more comprehensive discussion of the problem, including proofs, is provided in I. Goodfellow et al. (2014).

Subsequently, the GAN framework was extended to a conditional model (M. Mirza et al. 2014). This new model, known as “conditional GAN” or cGAN injects a conditioning variable y into both networks: the Generator now generates $G(z | y)$, and the Discriminator

evaluates $D(x | y)$. The adversarial objective becomes

$$V(D, G) = \mathbb{E}_{x, y \sim p_{data}(x)} [\log D(x|y)] + \mathbb{E}_{z, y \sim p_z(z)} [\log (1 - D(G(z|y)|y))] \quad (12)$$

The conditional variable y in a cGAN can be various additional information including images, labels or text contextual to “ground truth” real data x . Among various types of cGANs, Pix2Pix GAN with its image-to-image translation design is suitable for the task at hand. In our work, we specifically use this conditional variable by choosing y to represent the ground-based intensity-interferometry (II) observation patterns: the Generator is trained to produce stellar surface images that not only look realistic but also conform to the measured II correlations, while the Discriminator judges realism *and* consistency with the II data.

During each training session of the Discriminator, it is presented with a series of real images (as seen in Fig. (5) and generated images taken in equal proportion. During the initial phases of its training, as the generated images are sampled from random distribution, the Discriminator finds it easy to distinguish between the real and the generated images. This produces a sharp initial dip in the Discriminator loss function. On the other hand, the Generator loss function, during the initial phases of its training is high due to the poor quality of its gener-

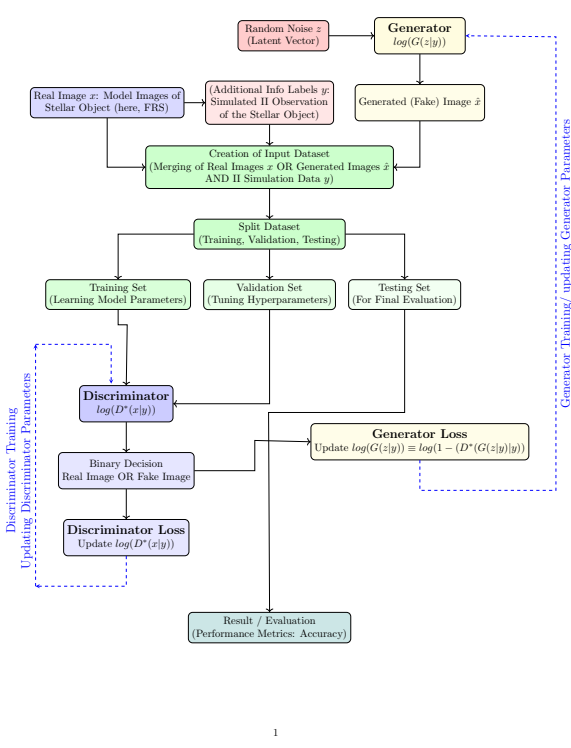


Figure 6. A schematic representation of the features of a cGAN model used in this work and the iterative process of its training, validation and testing. The process constitutes four broad stages: (1) choice of an appropriate GAN architecture including both the Discriminator and the Generator (not shown in this figure) (2) preparation of the Training, Validation and Testing datasets and (3) Training and Validation of the Model (4) Testing and Evaluation of the Model. The stages (2), (3) and (4) are depicted in this figure. The datasets are prepared in three broad steps: (i) generating the “ground truth” images of fictitious fast-rotators x , the sparse II images y used as the “condition” images in the Model and the generated images z sampled from a Normal Distribution (ii)merging these images into individual files with $(x|y)$ and/ or $(z|y)$ (as seen in an illustrated sample in Fig.(5)) and generating the full dataset in this process, and finally (iii) partitioning the full dataset into Training Set, Validation Set and the Testing Set. After the iterative training of the Model and its validation process is complete (“Nash point” of the Minimax Game is reached), the Model is tested using the Testing Set and evaluated.

ated images. Through the process of alternating training sessions, the Generator gradually learns to do better: generate images which resemble the real images ever more closely. As seen in fig. (7), with further training of both the networks, the Generator loss is gradually minimized and the generated images become gradually indistinguishable from the real images. The Discrimina-

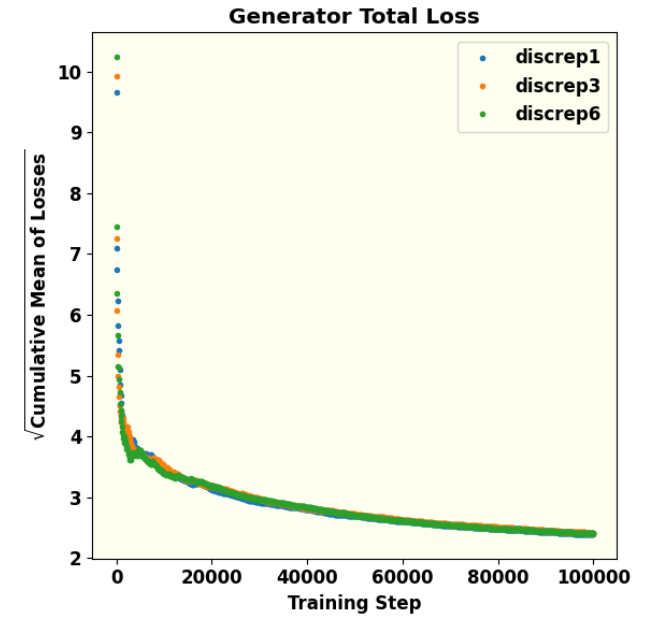
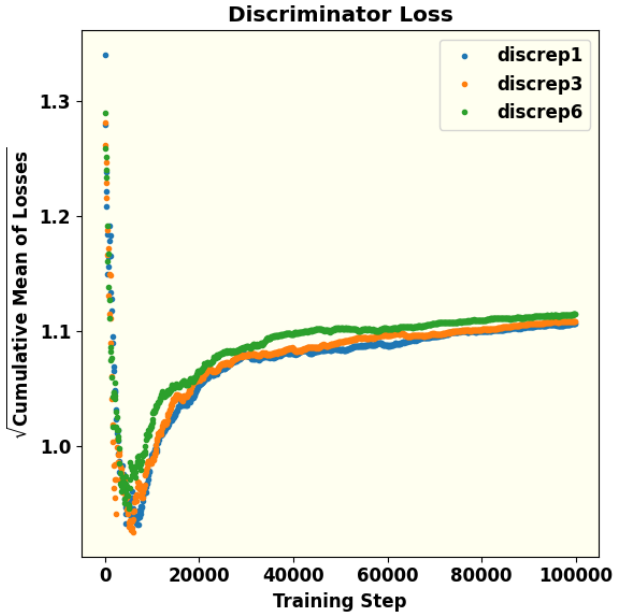


Figure 7. These figures show the effect of the ratio of episodes of Discriminator training per every episode of Generator training. This hyperparameter is termed Discriminator repetition or (discrep) in the figures. The square root of the cumulative mean of the losses are plotted against the training steps for 3 values of this ratio. Understandably, this ratio has a higher impact on the Discriminator loss than the Generator loss. Equal number of episodes of training produces minimum cumulative loss of the Discriminator. The dip in the Discriminator loss during the initial phases of its training can be interpreted as its early success in detecting “fake” (or generated) images because of a poorly trained Generator. With gradual training of the Generator, the success rate of the Discriminator decreases and eventually approaches saturation with equal probability of being successful in telling “fake” from real. The continual decrease and eventual saturation of the Generator loss is a result of its training to generate better images with increasing number of steps.

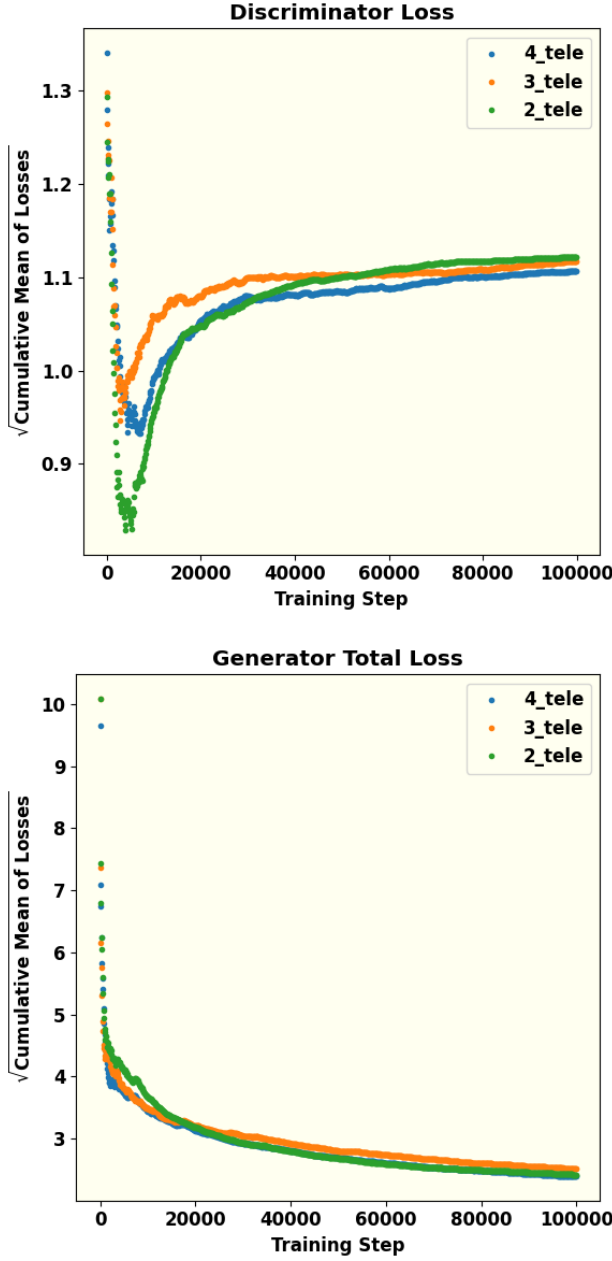


Figure 8. The square root of cumulative mean of Discriminator and Generator loss for different numbers of telescopes. The number of telescopes is also another hyperparameter that has significant impact on the model performance. If there are only two telescopes, both Discriminator and Generator are not trained smoothly. The result of four telescopes is a lot better because the cumulative mean of loss functions is smaller compare to other parameters. For the same reasons as explained in Fig.(7), we observe initial dip and eventual saturation of the Discriminator loss and continual decrease and eventual saturation of the Generator loss with training steps.

509 tor loss, on the other hand, increases from the minimum
510 of the initial phases of training and gradually saturates
511 to a value halfway between its maximum and minimum
512 values, as expected in the case of a binary classifier.

513 P. Isola et al. (2017) further observed that combining
514 the cGAN from Eq. (12) with the traditional $L_1(G)$ loss
515 (also known as the Mean Absolute Error) improves the
516 results, as the Generator is encouraged to produce out-
517 puts closer to the target image in a pixel-wise sense. We
518 adopt this approach in the training of our cGAN model
519 by including $L_1(G)$ defined in eq.(13)

$$520 \quad L_1(G) = \mathbb{E}_{x \sim p_{\text{data}}, z \sim p_z(z)} [\|x - G(z | y)\|_1]. \quad (13)$$

521 The total adversarial loss function, along with the L_1
522 loss modulated by a hyperparameter λ then becomes

$$523 \quad L_{\text{tot}} = \arg \min_G \max_D V(D, G) + \lambda \cdot L_1(G). \quad (14)$$

524 This type of network has demonstrated remarkable ro-
525 bustness across a variety of applications. For example, it
526 can generate colored images from grayscale inputs based
527 on architectural labels, transform images from day to
528 night, and even predict maps from satellite data. A more
529 extensive list of applications is provided in P. Isola et al.
530 (2017).

531 4.1. Generator

532 As discussed above, in a GAN the Generator, a deep
533 neural network in itself, is responsible for producing
534 synthetic data — in this case, images that resemble
535 those of a fast-rotating star. In this work, the Genera-
536 tor is implemented as a U-Net convolutional network (O.
537 Ronneberger et al. 2015). The U-Net consists of a sym-
538 metric encoder–decoder structure forming a characteris-
539 tic “U” shape along with skip connections: the left (con-
540 tracting or down-sampling) path, the right (expanding
541 or up-sampling path) and the connecting (bottle-neck)
542 path. The left down-sampling path repeatedly applies
543 3×3 convolutions (padded to preserve spatial dimen-
544 sions) followed by LeakyReLU activations and strided
545 convolution (with stride of 2), by progressively halv-
546 ing the spatial resolution while doubling the channel
547 depth (typically $64 \rightarrow 128 \rightarrow 256 \rightarrow 512 \rightarrow 1024$). At
548 the bottleneck, high-level features are processed with-
549 out further spatial reduction. The right up-sampling
550 path mirrors this process using 2×2 transposed con-
551 volutions (stride 2) for up-sampling, halving the channel
552 count at each level and using ReLU as the activation
553 function for all its layers except the output layer. Ad-
554 ditionally, a dropout layer is introduced at the begin-
555 ning of the upsampling phase to mitigate overfitting of
556 the Generator model (P. Isola et al. 2017). Critically,

long skip connections concatenate feature maps from each encoder (down-sampling) level to the corresponding decoder (up-sampling level), directly injecting high-resolution details into the reconstruction process. This enables the network to “remember where everything is” while the deep bottleneck still provides the large receptive field needed to think globally about image structure and semantics. Besides the strided convolutions, modern variants of U-Nets used in state-of-the-art GANs incorporate residual blocks within resolution levels, and frequently add spectral normalization and self-attention at the bottleneck for improved training stability and long-range dependency modelling. These architectural choices allow our U-Net generator to simultaneously recover sharp, high-frequency details (stellar limb edges, limb-darkening profiles, gravity darkening, and rapid-rotation-induced oblateness) and enforce global coherence (overall disk morphology and physical consistency with the observed interferometric visibilities)—making it ideally suited for high-fidelity sky-image reconstruction of fast-rotating stars from sparse ground-based intensity interferometry observations.

During the training, the total Generator Loss function L_G including the L_1 loss defined in eq.(13) that is minimized is given by

$$\begin{aligned} L_G = & -\mathbb{E}_{z \sim p_z(z)} [\log D(G(z | y) | y)] \\ & + \lambda \mathbb{E}_{x \sim p_{\text{data}}, z \sim p_z(z)} [\|x - G(z | y)\|_1]. \end{aligned} \quad (15)$$

Here,

- x denotes a real data sample (e.g. the “ground-truth” image; here, the synthetically generated fast rotator image) corresponding to condition y , the simulated II observation data.
- z is a random latent vector drawn from the prior $p_z(z)$.
- $G(z | y)$ is the generator output (the reconstructed / synthesized image) given z and condition y .
- $D(\cdot | y)$ is the discriminator’s estimate (probability) that its input is “real,” given the same condition y .
- λ is a hyperparameter controlling the trade-off between adversarial realism and pixel-wise fidelity (typical values depend on the problem — e.g. in pix2pix, $\lambda = 100$).

After generating images, the Generator aims to deceive the Discriminator into classifying the generated images as real. The extent to which the Generator succeeds in this deception is quantified by the GAN. When

the Discriminator is unable to distinguish between the generated and real images (i.e., when the GAN is minimized), the Generator is considered to have reached an optimal state. Conversely, if the generated image fails to fool the Discriminator, the Generator produces a new image for further comparison with the real image. Additionally, the Generator’s performance is evaluated using another metric known as the L_1 loss (defined in eqn. 13), which is defined as the mean absolute error between the pixels of the real image and those of the generated image. Balancing the minimization of both the GAN loss and the L_1 loss enables the Generator to produce images that are not only realistic but also faithful to the input data. In the training of the Generator network, a combination of these two loss functions, referred to as the Generator Total Loss L_{tot} and defined in eqn.(15) is minimized.

4.2. Discriminator

The Discriminator is tasked with classifying the images produced by the Generator as either real or fake. It takes a real image from the dataset (often referred to as the target image for the Generator) and provides feedback to guide the Generator toward producing more accurate images. In this work, the PatchGAN model (P. Isola et al. 2017) is employed as the Discriminator. Unlike a traditional global classifier, PatchGAN evaluates individual patches of the image, outputting a grid of predictions rather than a single scalar value. Each element in the grid corresponds to the “realness” of one patch of the image under examination of the Discriminator at a time. The final loss of the Discriminator is the average over all the patch responses. Evaluating the “realness” of the input image in terms of its constituent patches facilitates capture of texture/ style and other high frequency components in the image. As compared to a global discriminator, it also reduces the number of parameters in the network thereby helping reduce computation cost. It also works on images with arbitrary sizes.

Prior to the down-sampling of data using PatchGAN, each input image is preprocessed with application of Zero Padding followed by batch normalization. The purpose of Zero Padding is to prevent the loss of spatial information and to facilitate the extraction of deeper features from the down-sampled output. Batch normalization is required to stabilize the learning (loss minimization) process. PatchGAN then reduces the spatial dimensions of the images to extract localized features, ensuring the model focuses on smaller regions. In this down-sampling stage, a leaky version of the Rectified Linear Unit (LeakyReLU) is applied in the convolutional

654 layers, similar to the approach used in the Generator.
 655 The probability $D(\cdot | y)$ that the patch of the input image
 656 represented by \cdot is “real” is evaluated through this process.
 657 The loss function D of the full input image is obtained by averaging over all the patch responses.

658
 659 The Discriminator Loss function L_D that is optimized
 660 during the training process is given by

$$661 \quad L_D = -\mathbb{E}_{x \sim p_{\text{data}}(x|y)} [\log D(x | y)] \\ - \mathbb{E}_{z \sim p_z(z)} [\log (1 - D(G(z | y) | y))] \quad (16)$$

662 where the arguments of the D and G functions are as
 663 noted in the text following eq.(15) This loss is composed
 664 of two parts: one that assesses how accurately it iden-
 665 tifies fake images (by comparing predictions to a target
 666 value of 0) and the other that measures how accurately
 667 the Discriminator identifies real images (by comparing
 668 predictions to a target value of 1).

669 The training procedure of these two components of
 670 the cGAN model can be outlined as follows:

- 671 • The discriminator D is updated by minimizing
 672 L_D , keeping G fixed (so that D becomes better
 673 at distinguishing real vs generated images).
- 674 • The generator G is updated by minimizing L_G ,
 675 keeping D fixed — thus pushing G to generate
 676 images that are (a) judged “real” by D , and (b)
 677 close (in pixel-wise sense) to the ground-truth x .

678 The Discriminator’s architecture begins with an initial-
 679 izer that accepts both the input (generated) images
 680 and the corresponding real images. Initially, Salt-and-
 681 Pepper noise is added to the input images. PatchGAN
 682 then reduces the spatial dimensions of the images to ex-
 683 tract localized features, ensuring the model focuses on
 684 smaller regions. In this downsampling stage, a leaky
 685 version of the Rectified Linear Unit (LeakyReLU) is ap-
 686 plied in the convolutional layers, similar to the approach
 687 used in the Generator.

688 Subsequently, zero padding is applied, adding rows
 689 and columns of zeros around the images to prevent the
 690 loss of spatial information during convolution and to fa-
 691 cilitate the extraction of deeper features from the down-
 692 sampled output. Following this, batch normalization
 693 is employed to stabilize learning by normalizing acti-
 694 vations, and the Discriminator begins classifying each
 695 patch as real or fake. This is followed by additional lay-
 696 ers involving LeakyReLU activation, zero padding, and
 697 convolution, culminating in a final prediction that is fed
 698 to the Generator as feedback.

699 The effectiveness of the Discriminator is measured by
 700 its ability to distinguish between real and fake images,
 701 quantified through the Discriminator loss. This loss is

702 composed of two parts: one that measures how accu-
 703 rately the Discriminator identifies real images (by com-
 704 paring predictions to a target value of 1) and another
 705 that assesses how accurately it identifies fake images
 706 (by comparing predictions to a target value of 0). To-
 707 gether, these loss components ensure that the Discrimi-
 708 nator improves its classification performance, which in
 709 turn, challenges the Generator to produce increasingly
 710 realistic images.

711 5. NETWORK PARAMETERS

712 An appropriate cGAN architecture along with a set of
 713 hyperparameters was optimized by tuning. The objec-
 714 tive of the model, as already mentioned, was to learn to
 715 faithfully reproduce a set of sky-images of fast rotators
 716 subject to the condition that those images are consistent
 717 with their simulated II observation data. We discuss
 718 below the architecture and the hyperparameters of the
 719 cGAN model used for this task. Given the adversarial
 720 nature of GANs, where the Generator and Discrimina-
 721 tor engage in a minimax game, careful tuning of key
 722 parameters is critical to ensure that both networks are
 723 well-balanced for effective training.

724 5.1. Data Preparation

725 First, we simulate generate synthetic images of rapidly
 726 rotating stars by modelling them as oblate spheroids
 727 with varying radii and oblateness parameters between
 728 0.5 and 1. To incorporate the effect of gravity darkening,
 729 we also consider different viewing angles and assume a
 730 linear dependence on the declination angle of each point
 731 on the stellar surface. The traced ellipses result from
 732 integrating over the source’s hour angle. For hyperpar-
 733 ameter tuning and comparing different telescopes, the
 734 total observing duration is set to approximately 11.5
 735 hours. Finally, the ellipses are plotted, converted into
 736 grayscale images, resized, and stored as raw arrays to
 737 facilitate further analysis.

738 Next, Salt and Pepper noise is introduced into these
 739 images; usually this is done at the rate of 0.5% of the
 740 number of pixels in the image. Then, the images are re-
 741 sized and their mean is subtracted. A two-dimensional
 742 Fast Fourier Transform, along with a Fourier shift, is ap-
 743 plied, yielding a complex number for each pixel. Since
 744 II does not measure phase, the absolute value is calcu-
 745 lated. (as shown in Fig. 4 on both linear and logarithmic
 746 scales for visualization).

747 Next, sparse sampling of the interferometric plane is
 748 introduced via pixel-wise multiplication of the absolute-
 749 valued Fourier-transformed image (left panel of Fig. 4)
 750 and the sparse sampling map baseline tracks of (Fig. 2)
 751 generated by the four IACTs due to Earth rotation dur-
 752 ing the II observation. The result is a map in the Fourier

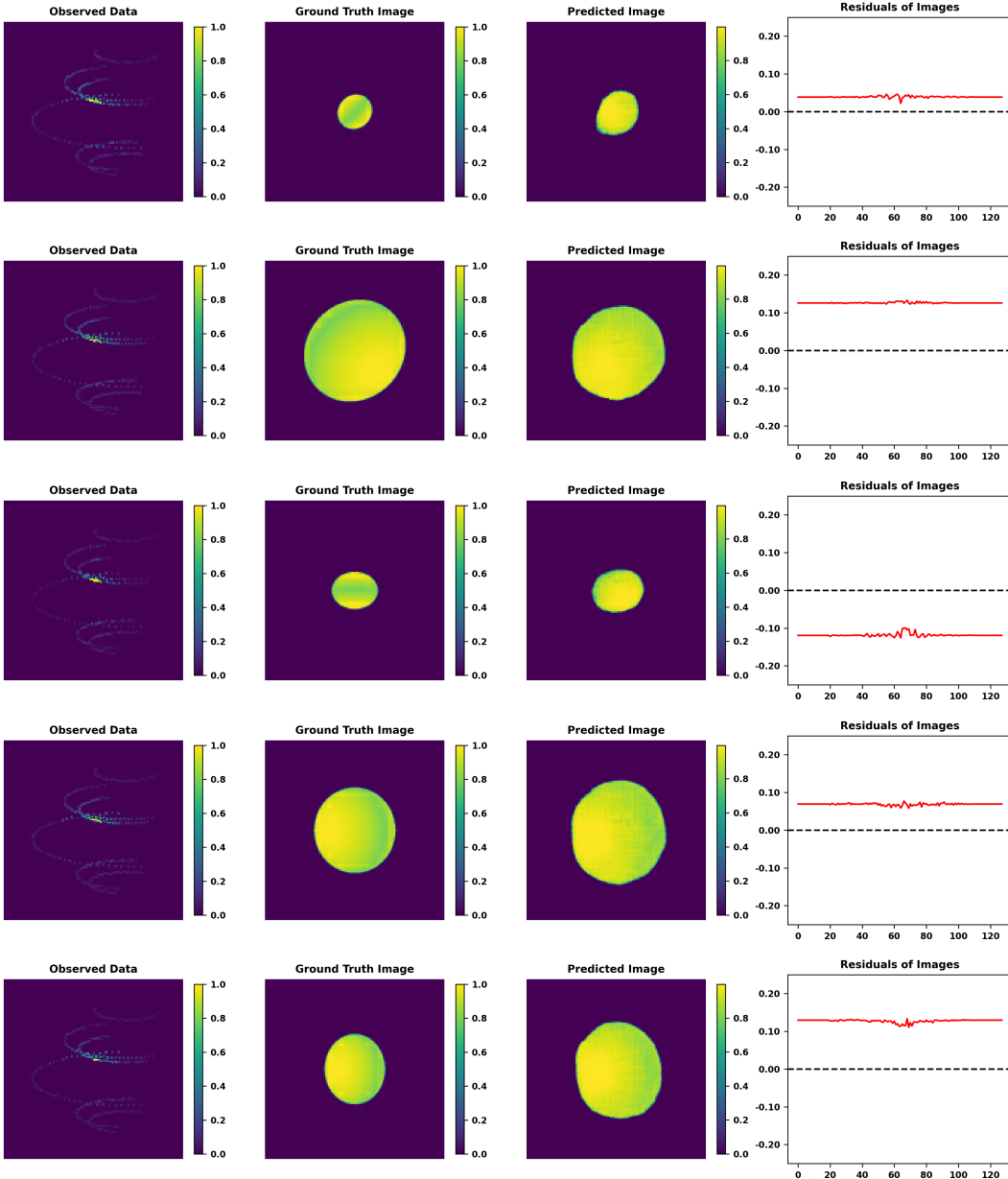


Figure 9. Example results of image reconstruction using the cGAN model along with the II observations simulated in this work. Each row in this figure represents the results for a hypothetical fast-rotating star. The left panel represents the sparse II pattern obtained by the simulated observation of the star using the four IACTs illustrated in Fig.1. This image acts as the “condition” part of the data input to the cGAN model. The second panel from left displays the real image, or ground truth, which the Discriminator uses to distinguish from the images generated by the Generator. The data generated for training, validation and testing of the cGAN model is a merge of this image and its II pattern presented in the left panel. The third panel is the reconstructed image, or the predicted image, produced by the trained GAN model . The fourth and the last panel is the difference between the ground truth and the predicted image in the (u, v) plane.

753 plane featuring several ellipses, which is also referred to
 754 as the sparse sampling map (right panel of fig. 4). This
 755 map represents the sparse sampling of the signal space
 756 corresponding to the source (Fig. 3) observed with four
 757 telescopes (Fig. 1). In essence, the right panel of fig. 4
 758 represents the result of simulated II observation of the
 759 fictitious fast-rotator illustrated in fig. 3.

760 Finally, we normalize the pixel values and convert
 761 them to 8-bit integers, producing an image that encodes
 762 the sparsely sampled, phase-free visibility measured by
 763 II. The image of the corresponding simulated (fictitious)
 764 star, which serves as the “ground truth” is processed
 765 identically to avoid any bias. These two images are
 766 merged side-by-side into a single image (as shown in
 767 Fig. 5). The dataset thus created is split into three
 768 parts in the proportions of 80% for training, 10% for
 769 validation, and 10% as the test set. This partition of
 770 the full dataset is indicated in the Fig.6. In the follow-
 771 ing, we refer to these three parts as the Training Set,
 772 the Validation Set and the Testing Set respectively.

773 Finally, the pixels are normalized and converted to 8-
 774 bit integers. This image represents the sparsely sampled
 775 phaseless visibility as it can be measured with II. The
 776 image shown in right panel of fig. 4 serves as the input
 777 for the GAN, which also requires the corresponding
 778 ground truth image. Consequently, the simulated stars
 779 are resized using the same algorithm and converted to 8-
 780 bit integers to reduce bias. The GAN must have access
 781 to the ground truth corresponding to each input image;
 782 therefore, the input and ground truth images are merged
 783 side-by-side (as shown in Fig. 5) and used to train the
 784 GAN. This procedure is applied to all simulated stars,
 785 with 10% used as test data, 10% as validation data, and
 786 the remaining 80% as training data.

787 5.2. GAN Architecture

788 The GAN architecture used in this work is a Pix2Pix
 789 cGAN, which uses an image-to-image translation strat-
 790 egy with both the ground truth and the condition being
 791 images. Originally introduced by Isola et al. P. Isola et
 792 al. (2017), this architecture is specifically suitable for
 793 image processing and reconstruction objectives. For in-
 794 stance, the TensorFlow tutorials⁶ demonstrate its applica-
 795 tion to a dataset of architectural facades. This archi-
 796 tecture has been adapted for the phase retrieval problem
 797 at hand here, some modifications are necessary. The
 798 network is implemented using the TensorFlow library
 799 (M. Abadi et al. 2016), calculations are performed with
 800 scipy (P. Virtanen et al. 2020), and plots are generated
 801 with matplotlib (J. D. Hunter 2007).

⁶ <https://www.tensorflow.org/tutorials/generative/pix2pix>

802 5.3. Hyperparameter Tuning

803 The cGAN model architecture used in this work em-
 804 ploys several hyper-parameters, which are explained
 805 briefly below (for a more in-depth discussion, see K. P.
 806 Murphy 2022).

807 The learning rate (lr) of the optimizer determines how
 808 much the model updates its parameters with each iter-
 809 ation. A learning rate that is too small may lead to under-
 810 fitting, while one that is too large can render the model
 811 unstable. Therefore, selecting an appropriate learning
 812 rate is crucial (K. P. Murphy 2022). A canonical choice
 813 in Pix2Pix and other GAN models is $lr = 2 \times 10^{-4}$. In
 814 our case too, we found this choice to be appropriate.

815 The kernel size refers to the dimensions of the con-
 816 volutional kernel used in the network, determining how
 817 many pixels are combined to produce a new pixel. A
 818 larger kernel size can capture features spanning several
 819 pixels, but it may also incorporate unrelated features.
 820 Small kernel sizes are preferable in cases where target
 821 images finer details or high spatial frequency features.
 822 Since the “ground truth” target images in our case have
 823 longer scale gravity darkening features, we have opted
 824 for the more canonical choice of kernel size being 5.

825 The amount of noise is controlled by two parameters,
 826 “alpha” and “beta”, which indicate the percentage of
 827 pixels altered to either white or black, hence the term
 828 Salt and Pepper noise. Here, “alpha” is applied to the
 829 real image, while “beta” is applied to the generated im-
 830 age. Different ratios (“alpha/beta”) can lead to varying
 831 model performance; however, our results indicate that
 832 distinct noise rates do not significantly affect the loss
 833 functions.

834 The batch size defines the number of images processed
 835 simultaneously by the network. Smaller batch sizes have
 836 been observed to improve generalization (S. J. Prince
 837 2023). However, because a larger batch size significantly
 838 increases training time, a batch size of 1 is used. Besides,
 839 in Pix2Pix cGAN implementations found in literature
 840 this choice is found to be often preferred.

841 Buffer size of a Pix2Pix GAN refers to a small mem-
 842 ory of image pool of previously generated images. They
 843 are occasionally fed to the Discriminator in place of the
 844 freshly generated ones. This strategy of mixing old and
 845 new fakes mitigates the risk of mode collapse wherein the
 846 Discriminator tends to map all or large number of gener-
 847 ated images to only one or a few real “ground truth” im-
 848 age(s). We have chosen a fairly large buffer size (=1400)
 849 to protect the model against mode collapse.

850 In the training of GANs, one often-followed strategy
 851 to potentially boost performance is to give the Discrimi-
 852 nator an advantage by increasing its number of training
 853 steps epochs before returning to the Generator’s train-

854
855
856
857
858
859
860
861
862
863
864
865
866
867
868
869
870
871
872
873
874
875
876
877
878
879
880
881
882
883
884
885
886
887
888
889
890
891
892
893
894
895
896
897
898
899
900
901
902
903
904
905

ing. This hyperparameter is referred to as the Discriminator repetition (as seen in Table 1). While this can lower the Discriminator loss, as shown in Fig. 7, it also increases training time and leads to a slight rise in the Generator loss. In training our model, we did not notice any significant advantage derived from this strategy. Since the generated images did not noticeably improve with additional Discriminator training, we adopted the strategy of typically training both the networks with equal preference (Discriminator repetition = 1).

One domain specific hyperparameter of the cGAN model presented here is the Number of Telescopes N_T . The degree of sparse sampling of the intensity interferometric (II) image plane can be varied to provide the model with access to more number of active (non-zero) pixels. Increasing the number of telescopes results in more baselines and, consequently, more number of active pixels in the II image. Point to note here, is that the coverage of the Fourier interferometric plane (number of active pixels in the II image) scales with available number of baselines, and the latter scales quadratically with the number of telescopes. Fig. 8 shows the loss functions for different numbers of telescopes. There is a significant disparity in performance of the model: at the “Nash point”, both the loss functions are minimized for the case of four telescopes. This is partly because the relationship between telescopes and baselines is quadratic: the coverage of the Fourier plane of Intensity Interferometry (II) scales as square of the number of telescopes employed in the II observation. For example, the Fourier plane can be sampled along six tracks when using four telescopes, as compared to only one track if using only two telescopes. In the case of two telescopes, both the Generator and Discriminator exhibit less smooth training, as indicated by the outliers. Performance improves with three telescopes and becomes very promising with four. Overall, the degree of sparse sampling appears to have the most pronounced effect of all the hyperparameters.

The hyperparameter Output Channels refers to the number of channels in the generator output (e.g., 1 for grayscale, 3 for RGB). It is worthwhile to recall that the cGAN model constructed in this work is trained on “ground truth” target images and the simulated II data, both in grey scales as seen in Fig.5. It is natural that the output of this model will be in grey scales only. Therefore the value of this hyperparameter is set to 1. The choice of hyperparameter λ has been commented upon earlier.

An optimized set of hyperparameters is selected through an iterative process of training and validation. For a tentatively chosen set of the hyperparameters,

906
907
908
909
910
911
912
913
914
915
916
917
918
919
920
921
922
923
924
925
926
927
928
929
930
931
932
933
934
935
936
937
938
939
940
941
942
943
944

the model is trained using the Training Set until the both the Discriminator and the Generator loss functions are minimized. This model, thus trained along with its model parameters, is then passed through validation using the Validation Set. This cycle of training and validation is iterated till an optimal set of hyperparameters is arrived at. During each epoch of training of the model, both the Discriminator and the Generator networks are trained for 100,000 steps. Plots of the “Discriminator Loss” function and the “Generator Total Loss” function presented in Fig.7 and Fig.8 represent the results of this training for two of the hyperparameters, namely, the Disriminator repetition (“discrep”, in short) and the Number of telescopes, respectively. Obviously, the most compute-intensive part of this process is that of the training of the Model. The results of training and validation presented in this work were carried out on a CPU using two nodes, each with 96 threads and the entire process of training and validation required approximately 20 hours on the machine employed for this work. This iterative process of training and validation of the Model is represented schematically in the Fig.6. The chosen optimal set of hyperparameters is presented in the table Table-1. This optimized and trained Model is

Table 1. Selected hyperparameters used for training the model.

Hyperparameter	Value
Learning rate	2e-4
Kernel size	5
Alpha/Beta	1
Batch size	1
Buffer Size	1400
Discriminator repetition	1
Number of Telescope	4
Output Channels	1
Lambda	100

then subjected to testing and evaluation using the Testing Set. The results of this testing and evaluation is presented in the following section.

The Pix2Picx cGAN architecture along with the choice of the values of the hyperparameters mentioned in the Table -1 and used in the implementation of this architecture constitutes the cGAN model (hereinafter referred to as “the GAN Model” or simply “the Model”).

6. IMAGE RECONSTRUCTION: RESULTS AND EVALUATION

In this section, we examine the performance of the GAN Model whose architecture and choice of hyperparameters have been discussed above. We subject the

945 trained Model to the task of phase retrieval and image
 946 reconstruction on the Testing Dataset.

947 The hyperparameter values that produce the best per-
 948 formance in our Model are tabulated in Table 1. In this
 949 section, we begin by discussing phase retrieval using
 950 hyperparameters, as mentioned earlier, followed by an
 951 analysis in which multiple sources are trained simulta-
 952 neously. The best performance for image reconstruc-
 953 tion has been observed with a learning rate of $2 \cdot 10^{-4}$, a ker-
 954 nel size of 5×5 , and equal noise percentages (alpha/beta
 955 = 1) applied to both the original and generated images.
 956 A batch size of 1 is used, and equal training is provided
 957 to both the Discriminator and the Generator.

958 6.1. Visual Evaluation of Images Predicted by the 959 Model

960 Fig. 9 demonstrates the success of the trained Model
 961 in reconstructing the images of a sample of the fictitious
 962 fast-rotators drawn from the Testing Set using their Inten-
 963 sity Interferometry (II) observations. The Model was
 964 trained on the training datasets for 100,000 steps and
 965 subsequently tested on various validation datasets to
 966 produce predicted images of the stars. The training
 967 was performed on a CPU using two nodes, each with
 968 96 threads, and required approximately 20 hours. In
 969 Fig. 9, four combined images illustrate the Model’s per-
 970 formance in reconstructing the stars’ shape, size, and
 971 brightness distribution using II.

972 The four panels from left to right in each row of Fig. 9
 973 represent the following:

- 974 • The left panel shows the signals collected from six
 975 baselines, which serve as the input for the Gener-
 976 ator during training.
- 977 • The left panel represents the sparse II pattern ob-
 978 tained by the simulated observation using the four
 979 IACTs illustrated in Fig.1. As explained earlier,
 980 this image acts as part of the input, namely its
 981 “condition” part. This image acts as the condi-
 982 tion that the sky-images of the star generated by
 983 the Generator must conform to.
- 984 • The second panel from left displays the real image,
 985 or ground truth target image, which the Discrim-
 986 inator loss function uses to distinguish from the
 987 images generated by the Generator. During train-
 988 ing, the Model aims to keep minimum difference
 989 between these ground truth image and generated
 990 images.
- 991 • The third panel from left presents the recon-
 992 structed (or predicted) image corresponding to the
 993 ground truth (second panel) and generated by the

994 trained Model. The similarity of these two images
 995 indicates the success of the Model in its stated ob-
 996 jective of image reconstruction.

- 997 • The right panel shows the residuals between the
 998 ground truth target image and the predicted image
 999 in the interferometric plane. The small values are
 1000 indicative of the success of training the Model.

1001 The predicted images and the residuals presented in
 1002 the third and the fourth columns (from left) of Fig. 9
 1003 show encouraging results, accurately conveying visual
 1004 information about the source’s size, shape, and bright-
 1005 ness distribution across its surface fairly accurately.
 1006 This has been achieved on the basis of the input pro-
 1007 vided by II observation using only six baselines. How-
 1008 ever, Arguably, further improvements can be achieved
 1009 by increasing the number of telescopes to enhance the
 1010 coverage of the (u, v) plane. A closer examination of this
 1011 proposition might be able to contribute to the design
 1012 and instrumentation aspects in the existing and upcom-
 1013 ing CTAO. an ideal candidate for this approach.

1014 6.2. Evaluation of the Model using Moments

1015 The reconstructed images are visually compelling,
 1016 demonstrating the Model’s effectiveness in using II to
 1017 reconstruct images. However, visual assessment alone is
 1018 insufficient; statistical evaluation of the generated im-
 1019 ages in comparison with the ground truth images is nec-
 1020 essary to validate the results. We present here the re-
 1021 sults of our calculation and comparison of the moments
 1022 of distribution pixel brightness in the target “Ground
 1023 Truth” images and the “Predicted” images.

1024 Image moments capture key properties of the recon-
 1025 structed objects—such as shape, size, and intensity dis-
 1026 tribution—by quantifying features like position, orienta-
 1027 tion, and brightness distribution. By comparing the mo-
 1028 ments of the Model-generated images with those of the
 1029 ground truth, we can objectively assess the consistency
 1030 and accuracy of the reconstruction. This approach pro-
 1031 vides a reliable framework for evaluating reconstruction
 1032 quality, as image moments can reveal subtle differences
 1033 in geometric and intensity properties that might not be
 1034 apparent through visual inspection alone.

1035 The raw moment M_{ij} of an image is defined as (M.-K.
 1036 Hu 1962)

$$1037 M_{ij} = \sum_x \sum_y x^i y^j I(x, y) \quad (17)$$

1038 where $I(x, y)$ represents the intensity at pixel (x, y) . The
 1039 zeroth order raw moment, or monopole, represents the
 1040 total intensity of an image. It is computed by sum-
 1041 ming all pixel values across the image, yielding an over-
 1042 all intensity measure. In this context, analyzing the

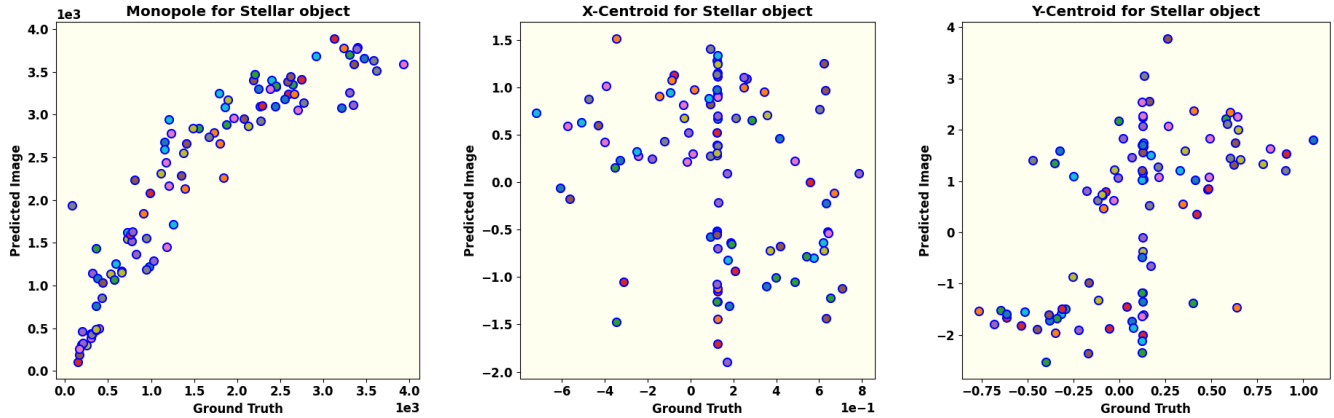


Figure 10. This set of figures shows comparisons of the monopole, and the coordinates of the centroids (x_c, y_c) of the pixel brightness distribution of the ground truth images and the corresponding images predicted (generated) by the trained model. The monopole moment of the images represents the overall pixel brightness of the images. The values, as expected of a trained Model, not only lie in same range, but lie close to the diagonal and show an approximate equality. The centroids of both the ground truth images and the predicted images lie within small ranges of pixel values as should be expected of an ideally trained model. Please see the relevant text for detailed comments.

monopole provides the total flux pixel brightness of the images of the fast-rotating fictitious stars. According to Eq. (17), the monopole of an image is calculated as:

$$M_{00} = \sum_x \sum_y I(x, y). \quad (18)$$

An ideally trained Model should predict the overall pixel brightness of the generated images to be in the same range of values, if not equal to those of the ground truth images. The left panel of Fig. 10 displays the monopole values for 100 reconstructed images. The plot reveals a broad agreement in the overall intensity of the ground truth targets and the predicted (generated) images. However, a slightly higher brightness of reconstructed images in the intermediate range of brightness is evident. This could, perhaps, be mitigated by tuning the Batch Size hyperparameter.

While the monopole effectively represents the total brightness, it does not provide information about the position, shape, size, or detailed brightness distribution of the fast-rotating stars. For these aspects, higher-order moments are necessary.

The first order raw moments normalized by the respective monopole moments of the images given by

$$\begin{aligned} x_c &= \frac{M_{10}}{M_{00}} = \frac{\sum_{x,y} x \cdot I(x, y)}{\sum_{x,y} I(x, y)} \\ y_c &= \frac{M_{01}}{M_{00}} = \frac{\sum_{x,y} y \cdot I(x, y)}{\sum_{x,y} I(x, y)} \end{aligned} \quad (19)$$

represent the centroids (x_c, y_c) of the pixel brightness distribution of the images. An ideally trained GAN model should produce the centroids of the target and predicted images within a small range of pixels. A larger range would imply a low fidelity in learning the brightness distribution of ground truth images. The middle and right panels of Fig. 10 compare the centroids (x_c, y_c) of 100 predicted images with their corresponding ground truths respectively. We notice that the coordinates of the centroids of ground truth images are spread across a range of 2 pixels whereas the those of the predicted images are spread across a span of 4 pixels along x -axis and 7 pixels along y -axis. This clustering of centroids within a small scale range across all results indicates that the reconstructed images represent the spatial distribution of brightness of predicted and ground truth images fairly accurately.

The “center of mass” of the sky image of any stellar object, is determined by its centroid, which provides the x and y coordinates representing the spatial position of the image. This centroid is computed using the first-order raw moments in conjunction with the monopole (the zeroth-order moment). The formulations for the centroid along the x and y directions are given by:

$$\begin{aligned} x_c &= \frac{M_{10}}{M_{00}} = \frac{\sum_{x,y} x \cdot I(x, y)}{\sum_{x,y} I(x, y)} \\ y_c &= \frac{M_{01}}{M_{00}} = \frac{\sum_{x,y} y \cdot I(x, y)}{\sum_{x,y} I(x, y)} \end{aligned} \quad (20)$$

Here, $I(x, y)$ represents the intensity at pixel (x, y) , M_{00} is the monopole (total intensity), and M_{10} and M_{01} are

1100 the first-order raw moments along the x and y axes
 1101 respectively. This formulation accurately captures the
 1102 spatial “center of mass” of the stellar object in the im-
 1103 age.

1104 The middle and right panel of Fig. 10 compare the
 1105 centroids (x_c, y_c) of 100 predicted images with their cor-
 1106 responding ground truths respectively. The clustering
 1107 of centroids within a specific scale range across all re-
 1108 sults indicates that the reconstructed images accurately
 1109 represent the spatial location of the fast-rotating star
 1110 relative to the ground truth.

1111 Furthermore, these calculated centroids are instru-
 1112 mental in analyzing the shape, size, and brightness dis-
 1113 tribution of the stars using higher-order image moments.
 1114 To this end, the central moment of an image is calcu-
 1115 lated according to:

$$1116 \mu_{pq} = \frac{1}{M_{00}} \sum_x \sum_y (x - x_c)^p (y - y_c)^q I(x, y). \quad (21)$$

1117 The sum of p and q defines the order of the central mo-
 1118 ment.

1119 **The second order central moment of the brightness**
 1120 **distribution of the images is analogous to the moment of**
 1121 **inertia of a mass distribution.** Fig. 11 presents the com-
 1122 **parison of second-order central moments** $(\mu_{11}, \mu_{20}, \mu_{02})$,
 1123 which are used to study the structure of a fast-rotating
 1124 star along the line of sight (as explained in the upcom-
 1125 ing subsection). All three plots demonstrate **an approxi-**
 1126 **mate equality** among these moments, similar to the
 1127 monopole, thereby confirming the success of applying
 1128 the Model to reconstruct images with II. **The small scat-**
 1129 **ter in the moments of the predicted images indicates**
 1130 **robust learning of the Model without over-fitting.**

1131 The third-order central moments $(\mu_{30}, \mu_{03}, \mu_{21}, \mu_{12})$ of
 1132 the images quantify the degree and direction of asymme-
 1133 try of the brightness distribution around their respective
 1134 centroids. Fig. 12 presents a comparison of all third-
 1135 order moments for both the ground truth and the recon-
 1136 structed image. All the four panels show a low skewness
 1137 in the brightness distribution of the ground truth im-
 1138 ages. The skewness of the predicted images along the
 1139 y -axis is dominated by one outlier as seen in the values of
 1140 μ_{03} and μ_{12} . However, the approximately uniform dis-
 1141 tribution of skewness of the predicted images along the
 1142 x -axis, with a few outliers though, as seen in the values of
 1143 μ_{30} and μ_{21} suggests that this feature in the ground
 1144 truth images has been picked up fairly well during the
 1145 training of the Model.

1146 **The brightness distribution is characterized by**
 1147 **the skewness of the image, which is quanti-**
 1148 **fied by calculating the third-order central mo-**
 1149 **ments** $(\mu_{30}, \mu_{03}, \mu_{21}, \mu_{12})$. Fig. 12 presents all

1150 **third-order moments for both the ground truth**
 1151 **and the reconstructed image.** The skewness
 1152 **along the x and y axes** (μ_{30} and μ_{03}) **appears**
 1153 **acceptable**, as shown in both upper panel of
 1154 **Fig. 12**, where a linear relationship exists be-
 1155 **tween the ground truth and predicted images.**
 1156 **However**, the other higher-order moments (μ_{21}
 1157 **and** μ_{12})—particularly μ_{12} , as depicted in both
 1158 **lower panel of Fig. 12**—**do not align as well.** This
 1159 **indicates that further improvement is possible**
 1160 **and should be investigated.**

1161 6.3. The reconstructed Parameters for object

1162 The centroids (x_c, y_c) indicate only the center of the
 1163 star and its spatial location in the image. In contrast,
 1164 the second-order central moments determine the ori-
 1165 entation, semi-major axis, and eccentricity relative to the
 1166 source’s center (M. R. Teague 1980). These moment-
 1167 based parameters fully describe the two-dimensional el-
 1168 lipse that fits the image data.

1169 The orientation of a fast-rotating star along the line of
 1170 sight is defined in terms of second-order central moments
 1171 as

$$1172 \theta = \frac{1}{2} \arctan \left(\frac{2\mu_{11}}{\mu_{20} - \mu_{02}} \right). \quad (22)$$

1173 The semi-major and semi-minor axes of the stellar ob-
 1174 ject are computed using the second-order central mo-
 1175 ments and are denoted as a and b , respectively.

$$1176 a = 2\sqrt{mp + \delta} \quad (23) \\ b = 2\sqrt{mp - \delta}$$

1177 where,

$$1178 mp = \frac{\mu_{20} + \mu_{02}}{2} \quad (24)$$

1179 and

$$1180 \delta = \frac{\sqrt{4\mu_{11}^2 + (\mu_{20} - \mu_{02})^2}}{2}. \quad (25)$$

1181 Using the calculated axis values, the eccentricity of the
 1182 fast-rotating star is determined as:

$$1183 e = \sqrt{1 - a/b}. \quad (26)$$

1184 Eqs. 22-26 describe the elliptical nature of the stellar
 1185 object (in this case, a fast-rotating star) and provide in-
 1186 formation on its shape and size, depending on the com-
 1187 puted values. In contrast, the brightness distribution
 1188 is characterized by skewness, which is quantified using
 1189 third and higher-order moments.

1190 7. CONCLUSION

1191 Intensity Interferometry (II) is re-emerging as a
 1192 promising technique to overcome the challenges of very

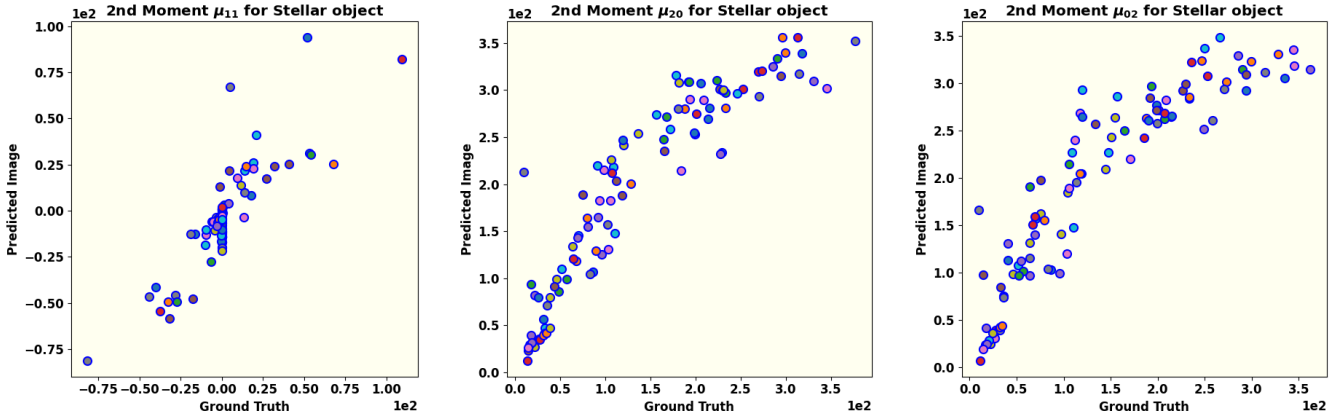


Figure 11. The second order central moment of the brightness distribution of the images is analogous to the moment of inertia of a mass distribution. The panels of this figure show the comparison of the second order moments (μ_{11} , μ_{20} , and μ_{02}) of the predicted images vs. the ground truth images from left to right respectively. Approximate equality of these moments is evident. The small scatter in the moments of the predicted images is indicative of a balanced training of the Model.

long baseline interferometry in the optical wavelength range. However, compared to radio-interferometry, optical interferometry faces a major hurdle: photon correlation captures only the magnitude of the interferometric signal, resulting in a loss of phase information.

This work addresses the challenge of phase retrieval in II using a machine-learning technique, specifically a conditional Generative Adversarial Network (cGAN). Our study demonstrates that applying a cGAN to II data successfully recovers the size, shape, and brightness distribution of a fast-rotating star. The size, shape and brightness distribution of fast rotating stars can be recovered by a cGAN trained on the combined input of the sky-image of known sources along with their respective II data. In this training the sky-image acts as the real “ground truth” and the II data acts as the “condition”. The Discriminator of the cGAN model is trained to efficiently distinguish between the real images and fake (generated) images based on the “ground truth” images and the respective II data condition. The Generator is trained to generate progressively realistic images which are also consistent with the condition of the II data. The evaluation of the trained model is then carried out Evaluations based on by comparison of image moments of real images and generated images. Specifically, the monopole, second, and third-order moments are compared. The results support the effectiveness of cGAN in achieving the stated objective. accurate image reconstruction from a simulation of II from a single site with four telescopes.

While the results of this study highlight the significant potential of machine learning, and in particular the applicability of cGAN, for image reconstruction in II, sev-

eral aspects require further refinement. First, an important factor in the reconstruction process is the extent of Fourier plane coverage, which depends on the number of available telescopes and the total observing time. The reasonable success of this piece of work suggests that a network of higher number of telescopes providing higher number of baselines and greater coverage of the (u, v) plane signal, would play a critical role in projects of image reconstruction of more complicated stellar systems can be undertaken. Future work might explore different observatory layouts to assess their impact on image reconstruction quality. Second, detector efficiencies, which impact the signal-to-noise ratio (SNR) of actual observational data, have not yet been incorporated; addressing these factors will be crucial for more accurate SNR estimation. Third, exploring and comparing alternative methods for image generation could reveal approaches that outperform cGAN in reconstructing stellar images with II. Fourth, experimenting with different loss functions could provide additional insights into the reconstruction quality. Although further testing is needed to refine the GAN and enhance its robustness and reliability, our findings suggest that machine learning is a promising approach for phase reconstruction in II.

ACKNOWLEDGEMENTS

Acknowledgment: One of the authors (SS) gratefully acknowledges the computing facilities and the local hospitality extended to him by the Inter-University Centre for Astronomy and Astrophysics (IUCAA), Pune, India under its Visiting Associate Programme during the preparation and finalization of this manuscript.

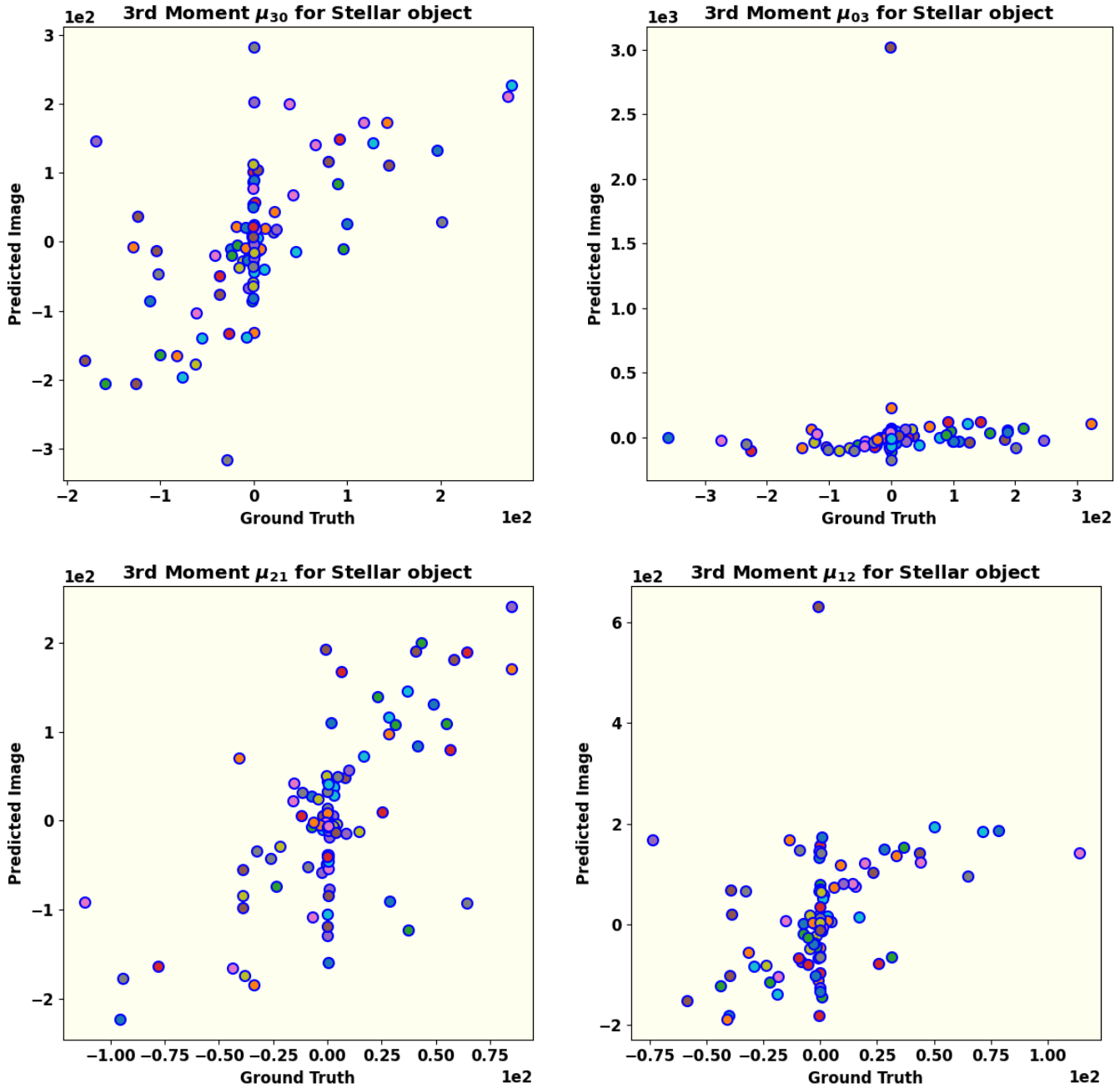


Figure 12. Shown here are all the third-order central moments (μ_{30} , μ_{03} , μ_{21} , and μ_{12}) for ground truth and predicted images generated by the trained Model. They represent the skewness of the brightness distributions. The low skewness in the brightness distribution of the ground truth images is evident. One outlier among the predicted images dominates their skewness distribution along the y -axis as seen in the values of μ_{03} and μ_{12} . The trained Model, however, seems to have learned the approximately uniform distribution of skewness along the x -axis as is evident, with a few outliers though, in the values of μ_{30} and μ_{21} .

REFERENCES

- 1257 Abadi et al., M. 2016, arXiv preprint arXiv:1603.04467 1260 Acharyya et al., A. 2024, The Astrophysical Journal, 966,
 1258 Abe et al., S. 2024, MNRAS, 529, 4387 1261 28
 1259 Acciari et al., V. A. 2020, MNRAS, 491, 1540 1262 Aleksić et al., J. 2016, Astroparticle Physics, 72, 76

- 1263 Archer, A., Aufdenberg, J. P., Bangale, P., et al. 2025,
 1264 arXiv e-prints, arXiv:2506.15027,
 1265 doi: [10.48550/arXiv.2506.15027](https://doi.org/10.48550/arXiv.2506.15027)
- 1266 Baumgartner et al., S. 2020, MNRAS, 498, 4577
- 1267 Coccolini et al., D. 2021, arXiv preprint arXiv:2122.11578
- 1268 Domiciano de Souza, A., Kervella, P., Jankov, S., et al.
 1269 2003, Astronomy and Astrophysics, 407, L47,
 1270 doi: [10.1051/0004-6361:20030868](https://doi.org/10.1051/0004-6361:20030868)
- 1271 Domiciano de Souza, A., Kervella, P., Jankov, S., et al.
 1272 2005, Astronomy and Astrophysics, 442, 567,
 1273 doi: [10.1051/0004-6361:20042476](https://doi.org/10.1051/0004-6361:20042476)
- 1274 Dravins et al., D. 2013, Astroparticle Physics, 43, 331,
 1275 doi: [10.1016/j.astropartphys.2012.04.017](https://doi.org/10.1016/j.astropartphys.2012.04.017)
- 1276 Fienup, J. 1982, Applied Optics, 21, 2758
- 1277 Gamo, H. 1963, Journal of Applied Physics, 34, 875
- 1278 Gerchberg, R. W. 1972, Optik, 35, 237
- 1279 Glauuber, R. J. 1963, Physical Review, 130, 2529
- 1280 Goldberger et al., M. L. 1963, Physical Review, 132, 2764
- 1281 Goodfellow et al., I. 2014, Advances in neural information
 1282 processing systems, 27
- 1283 Hanbury Brown, R., & Twiss, R. Q. 1956, Nature, 177, 27
- 1284 Hanbury Brown et al., R. 1957, Proceedings of the Royal
 1285 Society of London. Series A. Mathematical and Physical
 1286 Sciences, 242, 300
- 1287 Hanbury Brown et al., R. 1958, Proceedings of the Royal
 1288 Society of London. Series A. Mathematical and Physical
 1289 Sciences, 243, 291
- 1290 Hanbury Brown et al., R. 1974, Monthly Notices of the
 1291 Royal Astronomical Society, 167, 121
- 1292 Haubois et al., X. 2009, Astronomy & Astrophysics, 508,
 1293 923, doi: [10.1051/0004-6361/200912927](https://doi.org/10.1051/0004-6361/200912927)
- 1294 Holmes et al., R. 2010, in Adaptive Coded Aperture
 1295 Imaging, Non-Imaging, and Unconventional Imaging
 1296 Sensor Systems II, Vol. 7818, SPIE, 175–185
- 1297 Hu, M.-K. 1962, IRE transactions on information theory, 8,
 1298 179
- 1299 Hunter, J. D. 2007, Computing in Science & Engineering, 9,
 1300 90, doi: [10.1109/MCSE.2007.55](https://doi.org/10.1109/MCSE.2007.55)
- 1301 Isola et al., P. 2017, in Proceedings of the IEEE conference
 1302 on computer vision and pattern recognition, 1125–1134
- 1303 Kirisits et al., C. 2024, arXiv preprint arXiv:2406.14143v2
- 1304 Le Bohec, S; Holder, J. 2006, The Astrophysical Journal,
 1305 649, 399
- 1306 Li et al., X. 2014, in Imaging Spectroscopy, Telescopes and
 1307 Large Optics, Vol. 9298, SPIE, 92981G1–G7
- 1308 Liu, L.-C., Wu, C., Li, W., et al. 2024, arXiv preprint,
 1309 arXiv:2404.15685, doi: [10.48550/arXiv.2404.15685](https://doi.org/10.48550/arXiv.2404.15685)
- 1310 Liu et al., L.-C. 2025, Physical Review Letters, 134, 180201,
 1311 doi: [10.1103/PhysRevLett.134.180201](https://doi.org/10.1103/PhysRevLett.134.180201)
- 1312 Lucy, L. B. 1967, Zeitschrift für Astrophysik, Vol. 65, p. 89,
 1313 65, 89
- 1314 Maeder, A. 1999, Astronomy & Astrophysics, 347, 185
- 1315 Martinez, A. O., Baron, F., Monnier, J. D., Roettenbacher,
 1316 R. M., & Parks, J. R. 2021, The Astrophysical Journal,
 1317 916, 60, doi: [10.3847/1538-4357/ac06a5](https://doi.org/10.3847/1538-4357/ac06a5)
- 1318 McAlister et al., H. A. 2005, The Astrophysical Journal,
 1319 628, 439
- 1320 Mirza et al., M. 2014, arXiv preprint arXiv:1411.1784
- 1321 Monnier, J. D., Zhao, M., Pedretti, E., et al. 2007, Science,
 1322 317, 342, doi: [10.1126/science.1143205](https://doi.org/10.1126/science.1143205)
- 1323 Murphy, K. P. 2022, Probabilistic machine learning: an
 1324 introduction (MIT press)
- 1325 Mustafa et al., M. 2019, Computational Astrophysics and
 1326 Cosmology, 6, 1
- 1327 Norris et al., R. P. 2021, The Astrophysical Journal, 919,
 1328 124, doi: [10.3847/1538-4357/ac0c7e](https://doi.org/10.3847/1538-4357/ac0c7e)
- 1329 Nuñez et al., P. D. 2010, in Optical and Infrared
 1330 Interferometry II, Vol. 7734, SPIE, 458–467
- 1331 Nuñez et al., P. D. 2012a, Monthly Notices of the Royal
 1332 Astronomical Society, 419, 172
- 1333 Nuñez et al., P. D. 2012b, Monthly Notices of the Royal
 1334 Astronomical Society, 424, 1006
- 1335 Pedretti, E., Monnier, J. D., ten Brummelaar, T., &
 1336 Thureau, N. D. 2009, New Astronomy Reviews, 53, 353,
 1337 doi: [10.1016/j.newar.2010.07.005](https://doi.org/10.1016/j.newar.2010.07.005)
- 1338 Prince, S. J. 2023, Understanding deep learning (MIT
 1339 press)
- 1340 Rai, K. N., Basak, S., Sarangi, S., & Saha, P. 2025,
 1341 Resonance, 30, 45, doi: [10.1007/s12045-025-1729-x](https://doi.org/10.1007/s12045-025-1729-x)
- 1342 Rai et al., K. N. 2021, Monthly Notices of the Royal
 1343 Astronomical Society, 507, 2813,
 1344 doi: [10.1093/mnras/stab2391](https://doi.org/10.1093/mnras/stab2391)
- 1345 Rai et al., K. N. 2022, Monthly Notices of the Royal
 1346 Astronomical Society, 516, 2864,
 1347 doi: [10.1093/mnras/stac2433](https://doi.org/10.1093/mnras/stac2433)
- 1348 Ronneberger et al., O. 2015, in Medical image computing
 1349 and computer-assisted intervention—MICCAI 2015: 18th
 1350 international conference, Munich, Germany, October 5–9,
 1351 2015, proceedings, part III 18, Springer, 234–241
- 1352 Sato et al., T. 1978, Applied optics, 17, 2047
- 1353 Sato et al., T. 1979, Applied Optics, 18, 485
- 1354 Sato et al., T. 1981, Applied Optics, 20, 2055
- 1355 Schwanski et al., K. 2017, MNRAS, 467, L110
- 1356 Teague, M. R. 1980, Josa, 70, 920
- 1357 Teague, M. R. 1983, Journal of Optical Society of
 1358 America, 73, 1434
- 1359 van Belle, G. T., Ciardi, D. R., Thompson, R. R., Akeson,
 1360 R. L., & Lada, E. A. 2001, The Astrophysical Journal,
 1361 559, 1155, doi: [10.1086/322340](https://doi.org/10.1086/322340)

- ¹³⁶² Virtanen et al., P. 2020, Nature methods, 17, 261
¹³⁶³ Vogel et al., N. 2025, MNRAS, 537, 2334
¹³⁶⁴ Von Zeipel, H. 1924, Monthly Notices of the Royal Astronomical Society, Vol. 84, p. 665-683, 84, 665
¹³⁶⁶ Zhang et al., J. 2020, Opt. Lett., 45, 3649
¹³⁶⁷ Zhao, M., Monnier, J. D., Pedretti, E., et al. 2009, The Astrophysical Journal, 701, 209,
¹³⁶⁸ doi: [10.1088/0004-637X/701/1/209](https://doi.org/10.1088/0004-637X/701/1/209)
¹³⁶⁹